A&A 481, 169–181 (2008)
DOI: 10.1051/0004-6361:20079014

Astronomy & Astrophysics

ATCA 3 mm observations of NGC 6334I and I(N): dense cores, outflows, and an UCH II region

H. Beuther[1], A. J. Walsh[2], S. Thorwirth[3], Q. Zhang[4], T. R. Hunter[5], S. T. Megeath[6], and K. M. Menten[3]

[1] Max-Planck-Institute for Astronomy, Königstuhl 17, 69117 Heidelberg, Germany
e-mail: beuther@mpia.de
[2] Centre for Astronomy, James Cook University, Townsville, QLD 4811 Australia
e-mail: Andrew.Walsh@jcu.edu.au
[3] Max-Planck-Institute for Radioastronomy, Auf dem Hügel 69, 53121 Bonn, Germany
e-mail: [sthorwirth;kmenten]@mpifr-bonn.mpg.de
[4] Harvard-Smithsonian Center for Astrophysics, 60 Garden Street, Cambridge, MA 02138, USA
e-mail: qzhang@cfa.harvard.edu
[5] NRAO, 520 Edgemont Rd, Charlottesville, VA 22903, USA
e-mail: thunter@nrao.edu
[6] Ritter Observatory, Department of Physics and Astronomy, University of Toledo, Toledo, OH 43606-3390, USA
e-mail: megeath@astro1.panet.utoledo.edu

Received 7 November 2007 / Accepted 11 January 2008

ABSTRACT

Aims. We investigate the dense gas, the outflows, and the continuum emission from the massive twin cores NGC 6334I and I(N) at high spatial resolution.
Methods. We imaged the region with the Australia Telescope Compact Array (ATCA) at 3.4 mm wavelength in continuum, as well as $CH_3CN(5_K–4_K)$ and HCN(1–0) spectral line emission.
Results. While the continuum emission in NGC 6334I mainly traces the UCHII region, toward NGC 6334I(N) we detect continuum emission from four of the previously identified dust continuum condensations that are of protostellar or pre-stellar nature. The $CH_3CN(5_K–4_K)$ lines are detected in all K-components up to energies of 128 K aboveground toward two protostellar condensations in both regions. We find line width increasing with increasing K for all sources, which indicates a higher degree of internal motions of the hotter gas probed by these high K-transitions. Toward the main mm and CH_3CN source in NGC 6334I, we identify a velocity gradient approximately perpendicular to the large-scale molecular outflow. This may be interpreted as a signature of an accretion disk, although other scenarios, e.g., an unresolved double source, could produce a similar signature. No comparable signature is found toward any of the other sources. HCN does not trace the dense gas well in this region but it is dominated by the molecular outflows. While the outflow in NGC 6334I exhibits a normal Hubble-law like velocity structure, the data are consistent with a precessing outflow close to the plane of the sky for NGC 6334I(N). Furthermore, we observe a wide ($\sim$15.4 km s^{-1}) HCN absorption line, much broader than the previously observed CH_3OH and NH_3 absorption lines. Several explanations for the difference are discussed. The fits-files of the 3.4 mm continuum images and of the HCN(1–0) and $CH_3CN(5_K–4_K)$ data-cubes are available in electronic form at the CDS via anonymous ftp to cdsarc.u-strasbg.fr (130.79.128.5) or via http://cdsweb.u-strasbg.fr/cgi-bin/qcat?J/481/169

Key words. techniques: interferometric – stars: early type – stars: formation – ISM: individual objects: NGC 6334I and I(N) – line: profiles

1. Introduction

The massive twin cores NGC 6334I and I(N) at a distance of 1.7 kpc in the southern hemisphere (Neckel 1978; Straw & Hyland 1989) have been subjected to investigations for more than two decades. The two regions are located at the northeastern end of the much larger molecular cloud/HII region complex NGC 6334 (e.g., Rodríguez et al. 1982; Gezari 1982; de Pree et al. 1995; Kraemer & Jackson 1999; Sandell 2000; Carral et al. 2002). The reason NGC 6334I (synonymous with NGC 6334F) and NGC 6334I(N) are so interesting from a comparison point of view is that they are only separated by approximately 1 parsec, hence they share a similar large-scale molecular environment, but they exhibit extremely different characteristics probably because they are at different evolutionary stages.

Both regions have been studied in considerable detail over the last decades; recent summaries of the past observations can be found, e.g., in Hunter et al. (2006), Beuther et al. (2007b), or Rodríguez et al. (2007). Here we just outline their main characteristics. NGC 6334I is a prototypical hot molecular core right at the head of a cometary ultracompact HII (UCHII) region (de Pree et al. 1995; Kraemer & Jackson 1995). It exhibits rich spectral line emission (McCutcheon et al. 2000; Thorwirth et al. 2003; Schilke et al. 2006), a bipolar outflow (Bachiller & Cernicharo 1990; Leurini et al. 2006) and H_2O, OH, CH_3OH class II and $NH_3(3,3)/(6,6)/(8,6)/(11,9)$ maser emission (Moran & Rodríguez 1980; Forster & Caswell 1989; Gaume & Mutel 1987; Brooks & Whiteoak 2001; Norris et al. 1993; Caswell 1997; Walsh et al. 1998; Beuther et al. 2007b; Walsh et al. 2007). In contrast to that, up to very recently NGC 6334I(N) was

considered a typical cold core since no mid-infrared and only faint near-infrared emission was detected (Gezari 1982; Tapia et al. 1996; Persi et al. 2005). Furthermore, weak cm continuum and class I and II CH_3OH maser emission was reported (Carral et al. 2002; Kogan & Slysh 1998; Caswell 1997; Walsh et al. 1998). The spectral line forest is considerably less dense compared to NGC 6334I (Thorwirth et al. 2003), however, a few species are stronger toward NGC 6334I(N) (Sollins & Megeath 2004; Walsh et al. in prep.). In addition, Megeath & Tieftrunk (1999) reported the detection of a molecular outflow in this region as well. In summary, both regions show signs of active star formation, however, the southern region NGC 6334I appears to be in a more advanced evolutionary stage than the northern region NGC 6334I(N).

To better characterize this intriguing pair of massive star-forming regions, we started a concerted campaign from cm to mm wavelengths with the Australia Telescope Compact Array (ATCA), the Submillimeter Array (SMA) and the Mopra single-dish telescope. The previous ATCA $NH_3(1,1)$ to (6, 6) line observations revealed compact warm gas emission from both regions (Beuther et al. 2005, 2007b), and temperatures estimated to exceed 100 K. While toward NGC 6334I(N) the low energy NH_3 lines showed only extended emission, the high energy lines finally revealed compact gas components. The $NH_3(6,6)$ line profile from NGC 6334I(N) allowed speculation about a potential accretion disk. CH_3OH was strong in absorption toward the southern UCHII region in NGC 6334I, indicative of expanding gas. In the mm continuum emission, Hunter et al. (2006) used the SMA to resolve several mm continuum sources toward both regions (4 in NGC 6334I and 7 in NGC 6334I(N)). Furthermore, Hunter et al. (in prep.) identified an additional SiO outflow in NGC 6334I(N) that has its orientation in northeast southwest direction, approximately perpendicular to the one previously reported by Megeath & Tieftrunk (1999).

Here we present 3.4 mm continuum and HCN/CH_3CN spectral line observations obtained with the new 3 mm facility at the ATCA. These observations shed light on the outflow and dense gas properties of both regions as well as on the continuum emission from the embedded protostellar objects and the UCHII region.

Table 1. Line parameters.

Line	Freq. [GHz]	E_u/k [K]	n^a_{crit} [10^5 cm^{-3}]
HCN(1−0), $F = 1-1$	88.630	4	32
HCN(1−0), $F = 2-1$	88.632	4	32
HCN(1−0), $F = 0-1$	88.634	4	32
$CH_3CN(5_4 - 4_4)$	91.959	128	7
$CH_3CN(5_3 - 4_3)$	91.971	78	7
$CH_3CN(5_2 - 4_2)$	91.980	42	7
$CH_3CN(5_1 - 4_1)$	91.985	20	6
$CH_3CN(5_0 - 4_0)$	91.987	13	6

For all observed lines the columns list (left to right) the species/quantum numbers, frequencies, upper level energy states E_u/k (k is the Boltzmann constant) and critical densities n_{crit}.
[a] The critical densities $n_{crit} = A/\gamma$ are calculated at 60 K (Einstein coefficient A and collisional rate γ). For HCN, A and γ are taken from LAMBDA (Schöier et al. 2005). For CH_3CN, A is calculated from $A = 0.3\lambda_{100}^{-3}\mu^2$ (λ_{100} in units of 100 μm and $\mu = 3.9$ debye), and the corresponding γ-values are from Pei & Zeng (1995b,a). For a line optical depth $\tau > 1$, n_{crit} has to be multiplied by $1/\tau$ (Tielens 2005).

Table 2. Synthesized beams θ and rms.

Line	θ [″]	1σ rms [$\frac{mJy}{beam}$]
NGC 6334I		
3.4 mm cont.	2.3″ × 1.6″	23
$CH_3CN(5_4-4_4)$, [−12,2] km s^{-1}[a]	2.2″ × 1.6″	7
$CH_3CN(5_4-4_4)$, 1.7 km s^{-1}[b]	2.2″ × 1.6″	11
HCN(1−0), [−25, −19] km s^{-1}[a]	2.6″ × 1.8″	19
HCN(1−0), [5, 19] km s^{-1}[a]	2.6″ × 1.8″	16
HCN(1−0), 1.7 km s^{-1}[b]	2.5″ × 1.8″	33
NGC 6334I(N)		
3.4 mm cont.	2.6″ × 1.8″	2.6
$CH_3CN(5_{k=0,1}-4_{k=0,1})$[a], [−12, 8] km s^{-1}	2.2″ × 1.6″	4.9
$CH_3CN(5_4-4_4)$, 1.7 km s^{-1}[b]	2.2″ × 1.6″	8.4
HCN(1−0), [−16, −6] km s^{-1}[a]	2.5″ × 1.8″	19
HCN(1−0), [4, 12] km s^{-1}[a]	2.5″ × 1.8″	15
HCN(1−0), 2.0 km s^{-1}[b]	2.5″ × 1.8″	26

[a] Integrated velocity regime.
[b] Channel maps with the given velocity resolution.

2. Observations

The two regions NGC 6334I and I(N) were observed in May 2006 during two nights with the ATCA in the H214 configuration that results in projected baselines between 14 and 73 kλ at 88 GHz. The weather conditions at Narrabri were excellent with approximate precipitable water vapor of ∼10 mm and measured system temperatures between 150 and 670 K. The phase reference centers were RA (J2000) $17^h20^m53\overset{s}{.}44$, Dec (J2000) −35°47′02″.2 for NGC 6334I and RA (J2000) $17^h20^m54\overset{s}{.}63$, Dec (J2000) −35°45′08″.9 for NGC 6334I(N). The velocities relative to the local standard of rest (v_{lsr}) for NGC 6334I and NGC 6334I(N) are ∼−7.6 and ∼−3.3 km s^{-1}, respectively. We observed the 3.4 mm continuum emission at 88.4 GHz with a bandwidth and spectral resolution of 128 and 1 MHz, respectively. The spectral range for the continuum was checked to be line-free based on previous Mopra single-dish observations of that region (Walsh et al., in prep.). During one night, simultaneously with the continuum emission, we observed the HCN(1−0) line at 88.632 GHz. In the second night, the $CH_3CN(5_K-4_K)$ transitions at ∼91.98 GHz were targeted averaging two polarizations to achieve better signal-to-noise ratio. For more details on the spectral lines, see Table 1. A good uv-coverage was obtained through regular switching between both sources and the gain calibrators 1742−289 and 1759−39. The channel separation of the HCN observations was 0.25 MHz (∼0.85 km s^{-1}) and slightly worse with 0.5 MHz (∼1.63 km s^{-1}) for CH_3CN because we had to cover a broader bandwidth due to the several K-components. Flux calibration was performed with observations of Uranus and is estimated to be accurate within 20%. The primary beam of the ATCA at the observing frequency is 36″ (*FWHM*). The data were reduced with the MIRIAD package. Applying different weightings for the line and continuum data – mostly uniform weighting for the compact continuum and CH_3CN emission and natural for the more extended HCN emission – the synthesized beams vary between the different maps. The achieved spatial resolution and 1σ rms values are given in Table 2.

3. Results and discussion

All of the targetted spectral lines with excitation levels above-ground, E_u/k, between 4 and 128 K (Table 1) and the 3.4 mm continuum emission were detected and mapped toward both

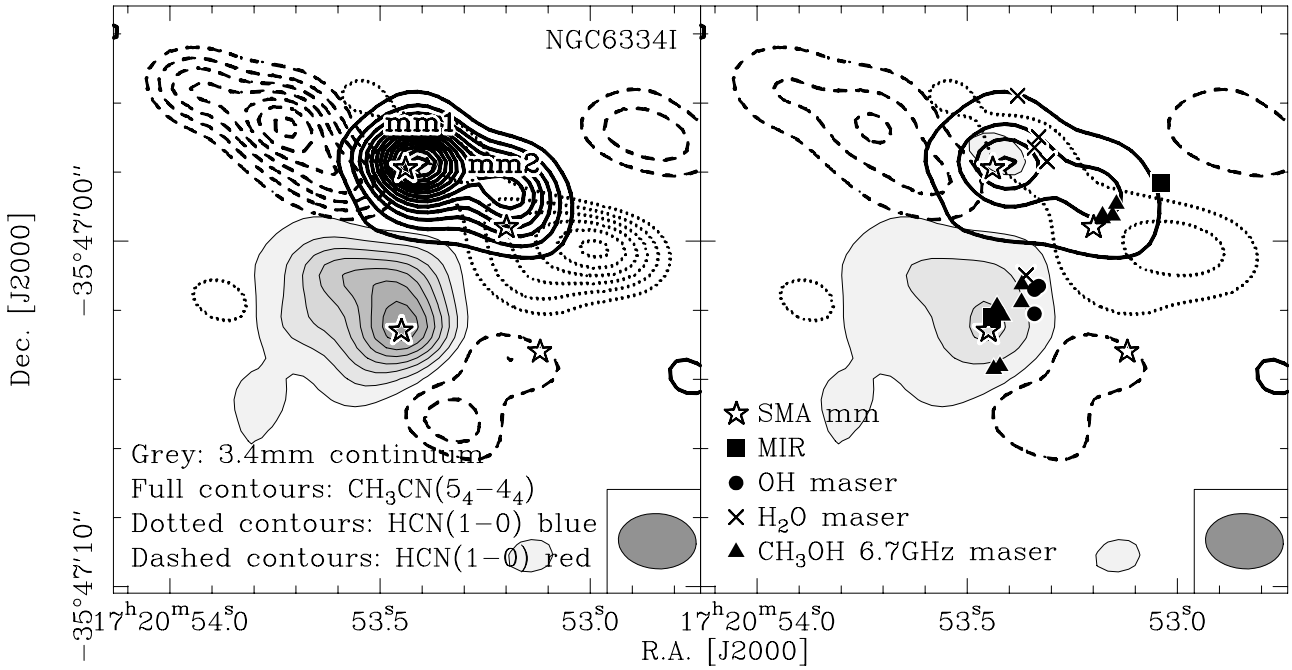

Fig. 1. 3.4 mm spectral line and continuum emission toward NGC 6334I: the grey-scale shows the 3.4 mm continuum and the full contours present the integrated $CH_3CN(5_4-4_4)$ emission from −12 to 2 km s^{-1}. The dashed and dotted contours show the blue- and red-shifted HCN(1−0) emission with integration ranges [−25, −19] and [5, 19] km s^{-1}, respectively. In the *left panel*, the 3.4 mm and CH_3CN emission is contoured from 3σ and continue in 3σ steps (1σ(3.4 mm) ∼23 mJy beam^{-1} and 1σ(CH_3CN) ∼7 mJy beam^{-1}). The red- and blue-shifted HCN contours start at 2σ and continue in 1σ steps (1σ(HCN−red) ∼19 mJy beam^{-1} and 1σ(HCN−blue) ∼16 mJy beam^{-1}). The mm sources from Hunter et al. (2006) are marked by stars. For clarity, the *right panel* shows the same data but with less contours, and additional poitions from various other observations are included (identified at the *bottom-left*). The corresponding references are: SMA mm continuum data from Hunter et al. (2006), H_2O masers from Forster & Caswell (1989), CH_3OH class II masers from Walsh et al. (1998), OH masers from Brooks & Whiteoak (2001), MIR sources from De Buizer et al. 2002). The $NH_3(6,6)/(8,6)/(11,9)$ are not shown but are spatially associated with mm2 (Beuther et al. 2007b; Walsh et al. 2007). The synthesized beam is shown at the bottom right of each panel.

target regions (Figs. 1 and 2). While CH_3CN is a typical hot core molecule and only detected toward the central warm protostars, HCN exhibits significantly more extended emission and shows a strong association with the various molecular outflows in the two regions. This may be considered surprising since the critical density of HCN(1−0) is even higher than that of CH_3CN. The 3.4 mm continuum emission is of different origin in both regions: while it is largely due to the free-free emission from the UCHII region in NGC 6334I, toward the northern region NGC 6334I(N) the continuum emission stems mainly from the dust in the vicinity of the embedded protostars. In the following we will outline the characteristics of both regions separately.

3.1. NGC 6334I

3.1.1. 3.4 mm continuum emission

Figure 1 presents an overlay outlining the main features of the spectral line and continuum emission toward NGC 6334I. Almost all of the 3.4 mm continuum emission arises from the UCHII region with a comparable morphology to the previous cm continuum images of that region (e.g., de Pree et al. 1995; Beuther et al. 2005). In contrast to that, it is only barely detectable at a 3.8σ level of 87 mJy beam^{-1} toward the strongest 1.4 mm continuum, NH_3 and CH_3CN peak position, mm1 in Fig. 1 (Hunter et al. 2006; Beuther et al. 2007b), marking the location of the dominating protostar in the region. Comparing this 3.8σ detection with the 1.4 mm data-point from Hunter et al. (2006) of 2.09 Jy beam^{-1} (the 1.4 mm data were re-imaged with the same beam-size as the 3.4 mm data), we get a spectral index of ∼3.4. However, since our detection is barely above the 3σ level, and mm1 may well harbor a so far undetected hypercompact HII region that could contribute still significant flux at 3.4 mm (e.g., Beuther et al. 2007a), we refrain from further analysis of that feature.

3.1.2. The dense gas observed in $CH_3CN(5_K-4_K)$

In contrast to the 3.4 mm continuum emission, the CH_3CN emission distribution shows the typical double-peaked morphology known from the previous NH_3 observations (Beuther et al. 2005, 2007b). The two CH_3CN peaks appear to be associated with the two strongest mm continuum sources (mm1 and mm2) in the region (Hunter et al. 2006). Figure 3 presents the full $CH_3CN(5_K-4_K)$ spectra extracted toward the two peak positions, and clearly all five K-components up to $K = 4$ with $E_u/k = 128$ K are well detected. Table 3 lists the fitted line parameters of the spectra.

Since the early work by Loren & Mundy (1984) CH_3CN has often been used as a thermometer to estimate rotation temperatures of the dense gas via Boltzmann plots assuming optically thin emission in local thermodynamic equilibrium (LTE). We tried this approach here as well, however, it failed because $CH_3CN(5_K-4_K)$ is optically thick. Similarly, we tried to model the CH_3CN spectra in LTE using the XCLASS superset to the CLASS software developed by Peter Schilke (priv. comm., see also Comito et al. 2005). This software package uses the line catalogs from JPL and CDMS (Poynter & Pickett 1985; Müller et al. 2001). However, this approach failed as well.

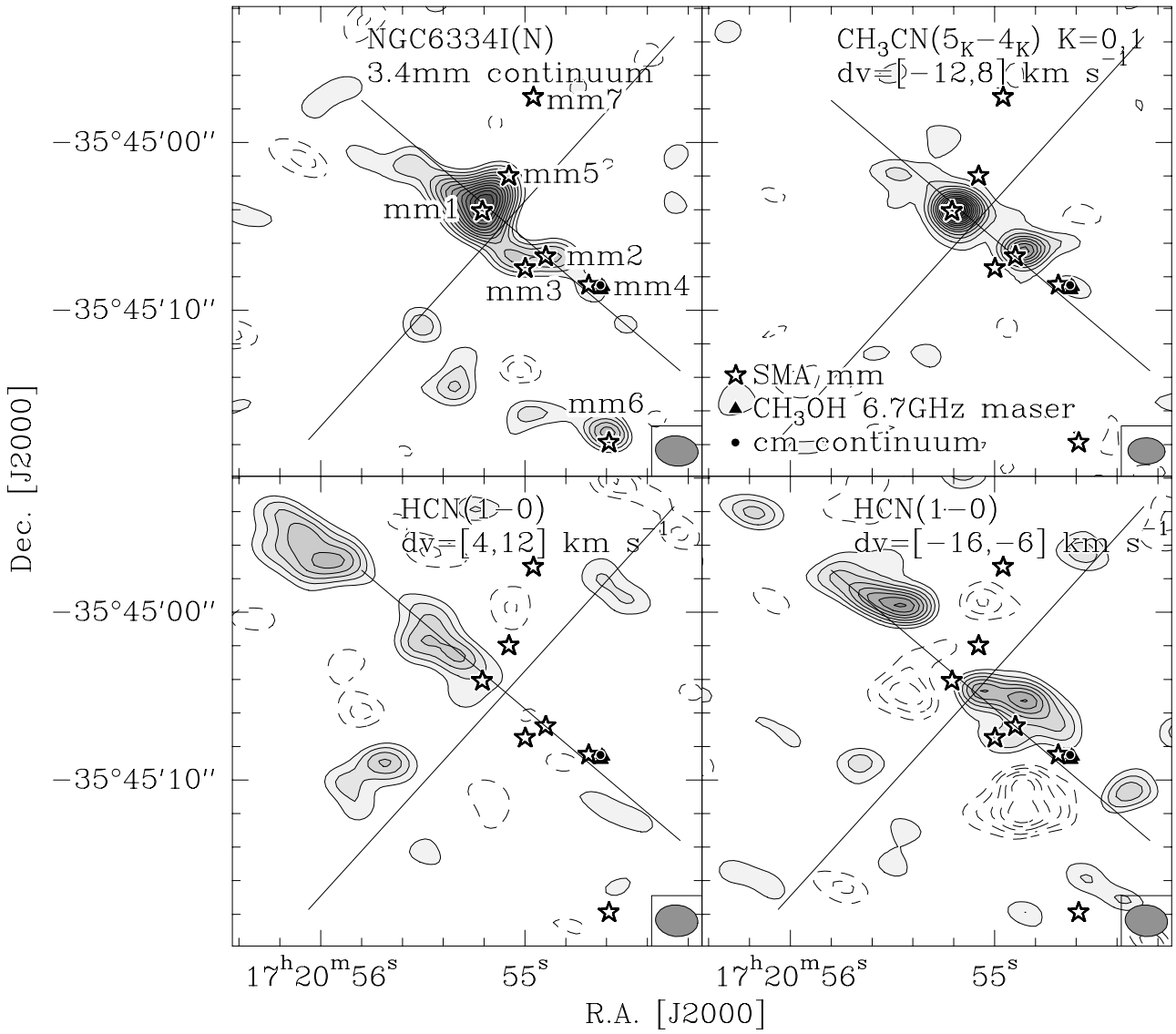

Fig. 2. 3.4 mm spectral line and continuum emission toward NGC 6334I(N). The four panels show the continuum (*top-left*), the integrated $CH_3CN(5_K{-}4_K)$ ($K = 0, 1$, *top-right*), and the red- and blue-shifted HCN(1−0) emission (*bottom-left* and *bottom-right* respectively). The velocity regimes are given in the figure. The 3.4 mm and CH_3CN emission is contoured from 2σ and continue in 2σ steps (1σ(3.4 mm) ∼2.6 mJy beam^{-1} and $1\sigma(CH_3CN)$ ∼4.9 mJy beam^{-1}). The red- and blue-shifted HCN wing contours start at 2σ and continue in 1σ steps (1σ(HCN−red) ∼19 mJy beam^{-1} and 1σ(HCN−blue) ∼15 mJy beam^{-1}). Negative features caused by insufficient uv-coverage are shown in dashed contours with the same levels as the emission. Markers of various other observations are identified in the top-right panel (SMA mm data from Hunter et al. 2006, the sources are labeled in the top-left panel, CH_3OH class II maser from Walsh et al. 1998, cm emission from Carral et al. 2002). The two lines outline the axes of the two molecular outflows identified by Megeath & Tieftrunk (1999), Hunter et al. (in prep.). The synthesized beams are shown at the bottom right of each panel.

Figure 3 shows a model spectrum at $T = 200$ K overlaid on the $CH_3CN(5_K{-}4_K)$ toward the main mm peak mm1. While the $K = 2, 3$ components still fit relatively well, the model reproduces neither the $K = 0, 1$ nor the $K = 4$ component. While this is partly again an opacity effect, it also shows that LTE is not appropriate for a source like NGC 6334I. As outlined below, different K-levels exhibit different line widths and hence do not trace the same gas components. Temperature gradients within the sources are imprinted in the spectra further complicating single-temperature fits. More sophisticated modeling of the CH_3CN emission is warranted. Although a few radiative transfer calculations of CH_3CN data exist (e.g., Olmi et al. 1993), the sparsely available collisional transition rates make such calculations a difficult task (the only partly available data are a small compilation by Pei & Zeng 1995b,a). Furthermore, in such hot and dense regions radiative excitation starts to matter which is hard to account for in any modeling approach.

While the full width half maximum (*FWHM*) line widths Δv for the two lowest energy lines of the $K = 0, 1$ components are less certain because of the line-blending between both components, one identifies a trend of increasing line width, Δv, with increasing K quantum number for $K \geq 2$ (Table 3). Figure 4 shows the Δv of $CH_3CN(5_K{-}4_K)$ for $K \geq 2$ toward the two CH_3CN peaks in NGC 6334I and I(N) plotted versus the level energy aboveground, E_u/k. For all four positions the trend of increasing Δv versus E_u/k is discernable. This trend indicates more internal motions from the warmer gas components (traced by the higher E_u/k lines) which perhaps originate from the inner warm regions close to the protostars. Similar to that, the bottom-panel of Fig. 5 shows the 2nd moment map of the $CH_3CN(5_4{-}4_4)$ line, i.e., its

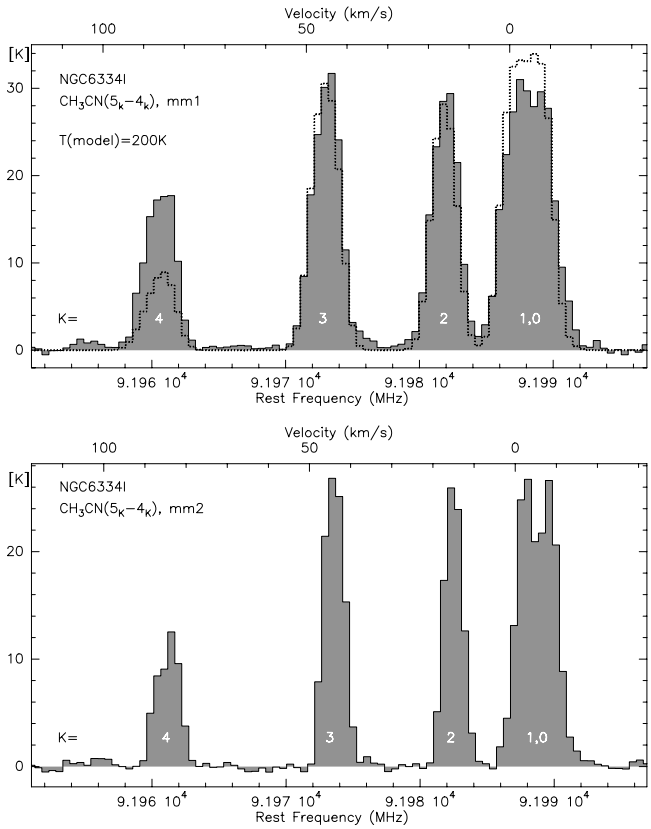

Fig. 3. $CH_3CN(5_K{-}4_K)$ spectra ($K = 0...4$) extracted toward the two CH_3CN peak positions in NGC 6334I shown in Fig. 1. The dotted line in the top panel shows a model spectrum created with XCLASS at a temperature of 200 K.

Table 3. Fitted $CH_3CN(5_K{-}4_K)$ line parameters.

Line	$S_{\rm peak}$ [K]	Δv^b [km s^{-1}]
NGC 6334I, mm1		
$CH_3CN(5_0{-}4_0)^a$	24.1	7.0 ± 0.4
$CH_3CN(5_1{-}4_1)^a$	27.8	8.3 ± 0.4
$CH_3CN(5_2{-}4_2)$	29.9	7.5 ± 0.2
$CH_3CN(5_3{-}4_3)$	31.9	7.8 ± 0.03
$CH_3CN(5_4{-}4_4)$	18.7	8.5 ± 0.1
NGC 6334I, mm2		
$CH_3CN(5_0{-}4_0)^a$	25.6	5.1 ± 0.3
$CH_3CN(5_1{-}4_1)^a$	26.9	5.3 ± 0.3
$CH_3CN(5_2{-}4_2)$	27.3	5.3 ± 0.1
$CH_3CN(5_3{-}4_3)$	28.8	5.8 ± 0.1
$CH_3CN(5_4{-}4_4)$	11.9	6.9 ± 0.2
NGC 6334I(N), mm1		
$CH_3CN(5_0{-}4_0)^a$	7.4	8.3 ± 0.6
$CH_3CN(5_1{-}4_1)^a$	6.9	8.4 ± 0.8
$CH_3CN(5_2{-}4_2)$	8.7	7.6 ± 0.5
$CH_3CN(5_3{-}4_3)$	8.9	7.7 ± 0.2
$CH_3CN(5_4{-}4_4)$	4.4	10.0 ± 0.4
NGC 6334I(N), mm2		
$CH_3CN(5_0{-}4_0)^a$	5.6	6.6 ± 1.0
$CH_3CN(5_1{-}4_1)^a$	5.7	3.9 ± 0.5
$CH_3CN(5_2{-}4_2)$	4.6	6.5 ± 0.5
$CH_3CN(5_3{-}4_3)$	4.5	6.0 ± 0.3
$CH_3CN(5_4{-}4_4)$	1.0	10.9 ± 1.6

[a] The fits to the $K = 0, 1$ lines are less accurate because of the strong line blending of both components.
[b] Full Width Half Maximum (*FWHM*).

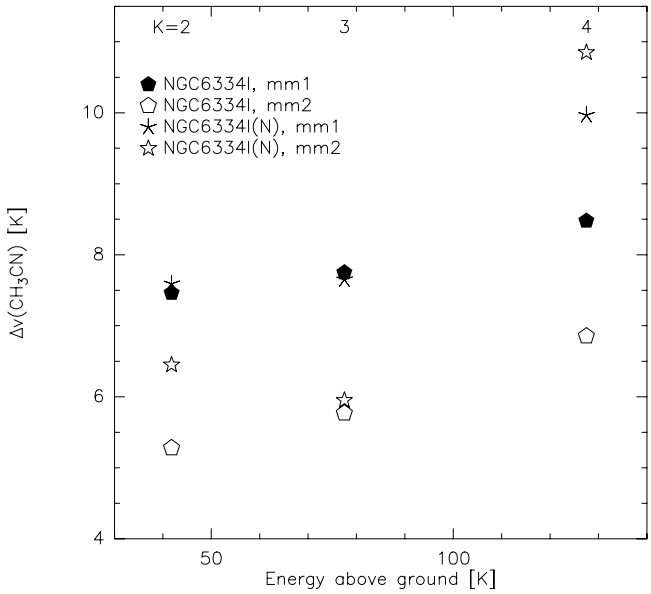

Fig. 4. Line widths $\Delta v(CH_3CN)$ from the various K-components plotted against the upper energy level of each line. We omitted the $K = 0, 1$ lines because of the line blending. The different symbols correspond to 4 different peak positions in NGC 6334I and I(N) as labeled in the plot. The corresponding errors are given in Table 3.

line-width distribution. Again we see the line width increase toward the center close to the main mm continuum peaks. Different processes may cause such line broadening, e.g., accretion disk rotation, infall or outflow motions. In particular, accretion disks are interesting candidates to explain such observational features.

To investigate rotation from a potentially embedded massive accretion disk, the top-panel of Fig. 5 presents the 1st moment map of the $CH_3CN(5_4{-}4_4)$ line, i.e., its peak velocity distribution. Although this structure is only barely resolved by the synthesized beam of 2.5″ × 1.8″ we tentatively identify a velocity gradient across mm1 with an approximate position angle (PA) of 113 ± 23 degrees from north. The same velocity structure is descernable in the lower $K = 3, 2$ CH_3CN transitions (we refrained from analyzing the $K = 0, 1$ lines because of their line-blending). To investigate this potential velocity gradient in more detail, we fitted the peak positions of each independent spectral channel (Fig. 6) which should allow us to increase the resolving power to approximately 0.5 HPBW/(S/N), where HPBW equals the synthesized beam and S/N the signal-to-noise ratio (Reid et al. 1988). Similar to the moment map, the case is not clear-cut, but nevertheless, the data are indicative of a velocity gradient with a PA of $\sim 134^{+20}_{-37}$ degrees from north. In comparison to these position angles, the PA of the previously identified molecular outflow is ∼46 degrees from north (Bachiller & Cernicharo 1990), which is approximately perpendicular to that found from our measurements, especially those from the highest-spatial-resolution position fitting (Fig. 6).

Based on these findings, we went back to the previous $NH_3(1,1)$ to $(6,6)$ observations (Beuther et al. 2005, 2007b) searching for similar signatures in these data. While the main hyperfine lines as well as the satellite lines of $NH_3(1,1)$ are dominated by the large-scale velocity gradient over the two main cores (e.g., Fig. 13 in Beuther et al. 2005), the satellite lines of the (J,K) lines with $J, K \geq 3$ are overlapping and difficult to image. However, the satellite hyperfine lines of the $NH_3(2,2)$ transition exhibit, in addition to the velocity gradient over the two cores, a second velocity gradient across mm1, again

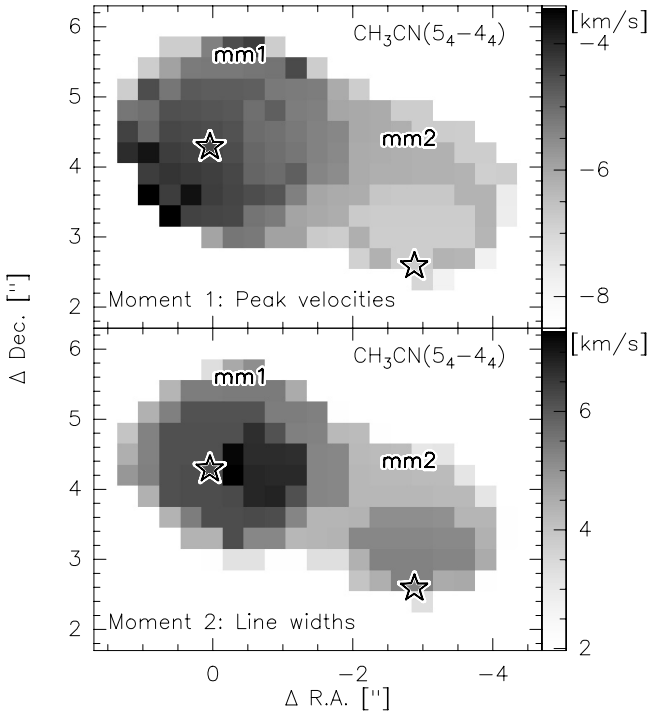

Fig. 5. Moment maps of $CH_3CN(5_4{-}4_4)$ toward NGC 6334I. *The top panel* shows the 1st moment (peak velocities) and *the bottom panel* the 2nd moment (line widths). The stars mark the positions of the two main mm continuum sources from Hunter et al. (2006). In addition to the velocity gradient from between mm1 and mm2, the 1st moment map exhibits a 2nd velocity gradient around mm1 in northwest southeast direction (approximately perpendicular to the large-scale outflow).

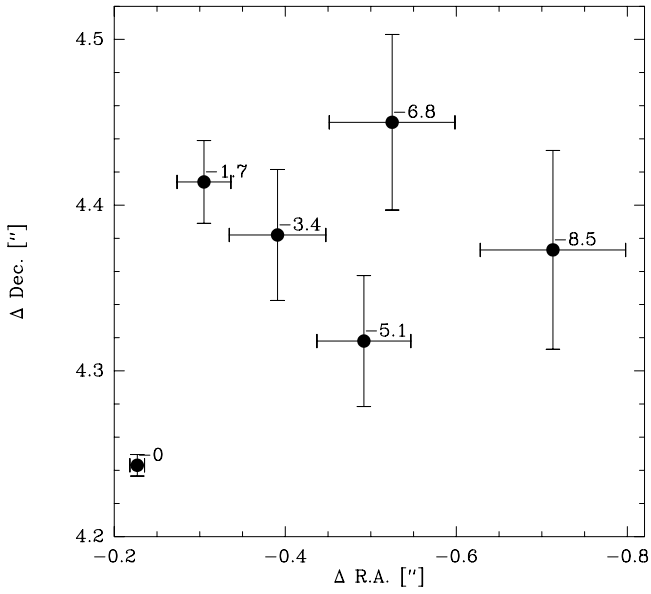

Fig. 6. Positional offsets around mm1 of the different CH_3CN $(5_4{-}4_4)$ velocity channels derived via Gaussian fits of the peak emission in each separate channel. The error-bars are the nominal 1σ errors from the fits, and the numbers label the central velocity for each position.

approximately perpendicular to the large-scale outflow (Fig. 7). The confirmation of this velocity gradient, first identified in the $CH_3CN(5_4{-}4_4)$ line, now in the lower opacity satellite hyperfine $NH_3(2,2)$ line supports its general credibility.

Since we do not resolve well the substructure of that velocity gradient to better investigate the kinematics (e.g., is there any Keplerian motion present?) the data do not allow the claim that a massive accretion disk was detected. For example, an unresolved double-source with different line-of-sight velocities could produce a similar signature (e.g., Brogan et al. 2007). Nevertheless, these observations are suggestive of a rotating structure perpendicular to the molecular outflow within a projected diameter of ∼0.33″ derived from Fig. 6. At the given distance of 1.7 kpc, this corresponds to a radius of the rotating structure of ∼280 AU. This scale fits well to the sizes of the accretion disks simulated recently via 3-dimensional radiative-transfer hydrodynamic calculations by Krumholz et al. (2007).

Adopting the proposed disk scenario, we can estimate the approximate rotationally supported binding mass $M_{\rm rot}$ assuming equilibrium between the centrifugal and gravitational forces at the outer radius of the disk. Then we get

$$M_{\rm rot} = \frac{\delta v^2 r}{G} \quad (1)$$

$$\Rightarrow M_{\rm rot}[M_\odot] = 1.13 \times 10^{-3} \times \delta v^2[{\rm km\,s^{-1}}] \times r[{\rm AU}] \quad (2)$$

r is the disk radius, and δv the half width zero intensity (HWZI) of the spectral line, approximately 5.1 km s^{-1} (half the velocity range shown in Fig. 6). Equations (1) and (2) have to be divided by $\sin^2(i)$ where i is the unknown inclination angle between the disk plane and the plane of the sky ($i = 90°$ for an edge-on system). With the given values we can estimate $M_{\rm rot}$ to $\sim 8/(\sin^2(i))\,M_\odot$. This is on the same order of the mass derived from the mm continuum emission (Hunter et al. 2006) which is assumed to stem largely from the disk/envelope system.

How do these masses correspond to the mass and luminosity of the central embedded source? While the bolometric luminosity of NGC 6334I is estimated to be $\leq 2.6 \times 10^5\,L_\odot$ (Sandell 2000), approximately $0.32 \times 10^5\,L_\odot$ are attributed to the UCHII region (based on the Lyman continuum flux presented in de Pree et al. 1995). One should keep in mind that this value may be a lower limit since dust could absorb a significant fraction of the uv-photons (Kurtz et al. 1994). The remaining $\leq 2.3 \times 10^5\,L_\odot$ has to be due to the various sources associated with the hot molecular core. Since the associated mid-infrared source to the west (Fig. 1) is of relatively low luminosity (only 67 $L_\odot$, De Buizer et al. 2002), it is likely that most of the luminosity stems from the two main continuum and spectral line peaks. In the extreme case, splitting the luminosity simply by two, it still implies that about $\leq 1.15 \times 10^5\,L_\odot$ emanate from the mm1 region. Assuming a ZAMS star, this corresponds to an embedded star of $\leq 30\,M_\odot$. In the above adopted accretion disk scenario, this would imply an inclination angle i between the disk plane and the plane of the sky of approximately 30 degrees. However, with the large uncertainties in the rotational mass and the central object mass estimate, such an inclination angle estimate should not be taken at face value, but only gives a rough idea that the system is neither edge- nor face-on. The comparable mass derived from the mm continuum emission (Hunter et al. 2006) indicates that a significant fraction of the total system mass stems from the proposed accretion disk and envelope. This implies that the rotating structure is unlikely in Keplerian motion but that it may be a self-gravitating structure and potential site of ongoing subfragmentation (see also comparable analytic calculations and hydro-simulations by, e.g., Kratter & Matzner 2006; Krumholz et al. 2007).

However, on a cautionary note, one has to keep in mind that the data are not conclusive as to whether we really see disk

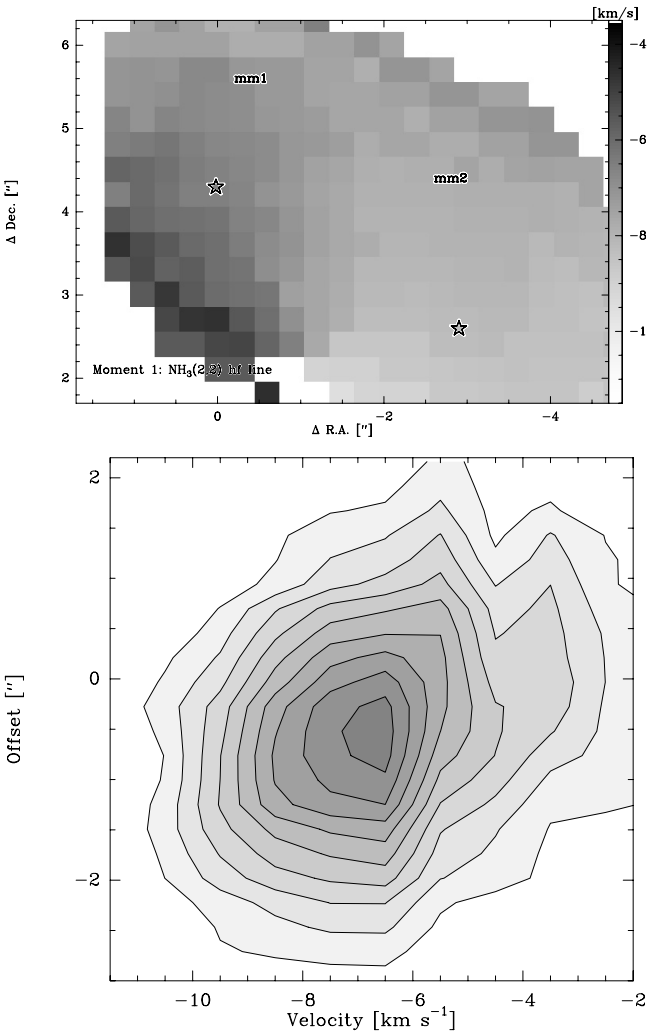

Fig. 7. First moment map (*top*) and position velocity diagram (*bottom*) of the the most blue-shifted satellite hyperfine line of $NH_3(2,2)$ toward NGC 6334I. The data are re-examined from Beuther et al. (2005). The position velocity digram is centered on mm1 with a position angle of 136 degrees from north. In addition to the velocity gradients between mm1 and mm2, the data exhibit a 2nd velocity gradient around mm1 in northwest southeast direction (approximately perpendicular to the large-scale outflow). The synthesized beam is $2.8'' \times 2.2''$.

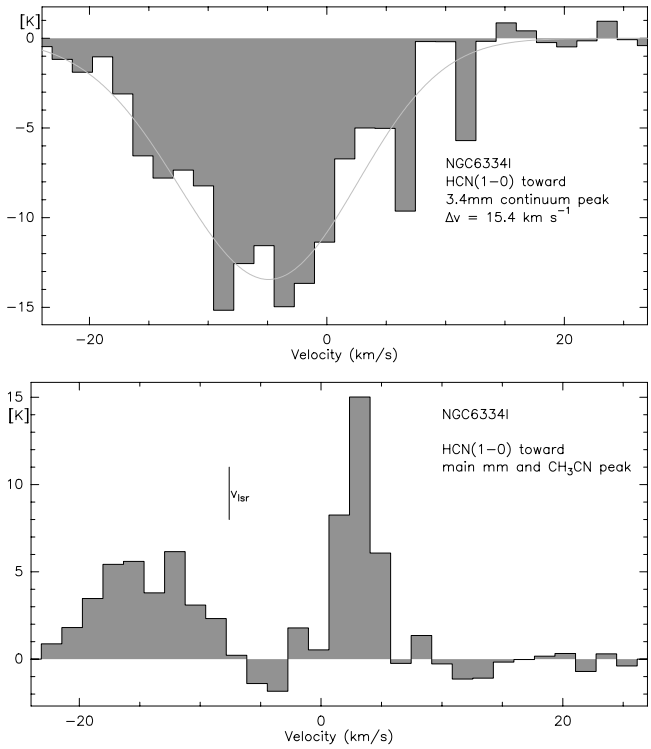

Fig. 8. HCN(1−0) spectra in NGC 6334I. *The top spectrum* shows the strong absorption toward the 3.4 mm continuum peak that coincides with the UCHII region previously observed at cm wavelengths. *The bottom spectrum* is extracted toward the main CH_3CN peak that coincides with the main mm continuum peak SMA1 by Hunter et al. (2006).

signatures or whether the observed gradient may be caused by other motions, e.g., an unresolved double-source.

3.1.3. The molecular outflow observed in HCN(1−0)

The blue- and red-shifted HCN(1−0) emission in Fig. 1 shows high-velocity emission associated with the molecular outflow in northeast southwestern direction (Bachiller & Cernicharo 1990; Leurini et al. 2006). The PA of the emission is not exactly the 45 degrees derived previously from the single-dish CO observations but it is closer to 65 degrees. However, such a discrepancy is not necessarily a surprise if one considers the missing flux problem we encounter in the HCN observations. Figure 8 (bottom panel) presents the HCN spectrum extracted toward the mm1 peak position, and while we see well the blue- and red-shifted emission, nearly all the flux around the $v_{\rm lsr}$ of $\sim -7.6\,{\rm km\,s^{-1}}$ is filtered out. This is also the reason we do not see HCN emission from the hot core itself, which is prominent in CH_3CN. Therefore, we just see some selectively chosen part of the outflow in HCN that could for example be associated with the limb-brightened cavity walls of the outflow which would explain the different apparent PA of the image. Figure 9 shows a position-velocity diagram centered at the main mm emission and CH_3CN peak mm1 along the apparent axis of the HCN emission. Again we find no emission around the systemic $v_{\rm lsr}$ but going to higher velocities, the blue- and red-shifted gas exhibits increasing velocity with increasing distance from the center, closely resembling the typical Hubble-law of molecular outflows (e.g., Lee et al. 2001). Such Hubble-law like behavior can be explained on the smallest jet-scales close to the protostar by the decreasing gravitational potential of the central star, however, on the larger scales we observe here this effect gets negligible and the Hubble-law of molecular outflows is explained by a density gradient decreasing with distance combined with the continuous (or episodic) driving of the jet that constantly induces energy in the outflow (e.g., Shu et al. 1991; Smith et al. 1997; Downes & Ray 1999).

Figure 10 (top panels) presents the 1st and 2nd moment map (intensity-weighted peak velocity and line-width distributions) of the HCN(1−0) emission. It is interesting to note that the line-width distribution clearly peaks toward the strongest mm continuum and molecular line source mm1 and that the large-scale HCN velocity gradient is approximately centered toward that position as well. This is indicative of a scenario which puts the driving source of the molecular outflow observed in HCN at this position. However, previous $NH_3(6,6)$ maser observations showed the maser peak position being associated with mm2 with additional features along the axis of the CO molecular outflow (Beuther et al. 2007b). These features were interpreted as indicative of this outflow being driven by a source associated with

Table 4. Line parameters for all absorption lines.

Line	E_u/k [K]	n_{crit} [cm^{-3}]	Δv [km s^{-1}]
$NH_3(1,1)$	24	2.1e3	1.4 ± 0.4
$NH_3(2,2)$	65	2.2e3	2.0 ± 0.3
$CH_3OH(3_{2,1}-3_{1,2})$	36	1.0e4	1.8 ± 0.1
$CH_3OH(4_{2,2}-4_{1,3})$	45	1.2e4	2.1 ± 0.1
$CH_3OH(2_{2,0}-2_{1,1})$	29	0.8e4	1.7 ± 0.1
HCN(1−0)	4	2.6e6	15.4 ± 0.3

The NH_3 and CH_3OH data are from Beuther et al. (2005). The listed parameters are the upper level excitation energies E_u/k, the critical densities n_{crit} calculated at 60 K and the observed line widths of the absorption lines toward the UCHII region peak position.

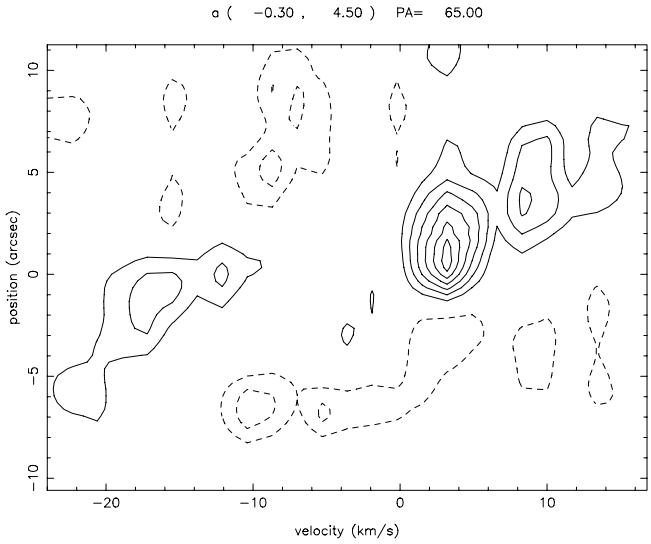

Fig. 9. Position-velocity diagram of HCN(1−0) in NGC 6334I along the main outflow axis. The cut is centered on the main CH_3CN peak at positional offset −0.3″/4.5″ with a position angle of 65° from north-to-east. Emission at the velocity of rest around −7.6 km s^{-1} is largely filtered out.

mm2. While the case is not clear-cut with two independent and different outflow driver indications, it is also possible that we are witnessing two different outflows observed in HCN and CO that may emanate from mm1 and mm2, respectively. In this scenario, mm1 could be the driver of a potentially denser and younger outflow that is better detected in HCN, whereas mm2 may be the driver of the larger, possibly older outflow observed in CO. Future observations at higher angular resolution and/or with different outflow tracers are required to assess the validity of this scenario.

3.1.4. Absorption toward the UCH II region

Another interesting feature of the HCN data is that we see strong absorption in the direction of the UCHII region, similar to the previously observed absorption in CH_3OH and NH_3 (Beuther et al. 2005). Figure 8 (top panel) shows the HCN(1−0) spectrum extracted toward the 3.4 mm continuum peak position. Fitting the HCN(1−0) line width, we take into account its hyperfine structure consisting of three lines (F = 0−1, 2−1, 1−1) with relative intensities of 1:5:3 in the optically thin limit and velocity shifts of −7.1, 0 and 4.9 km s^{-1}, respectively (Poynter & Pickett 1985). The line width Δv of that absorption feature is 15.4 km s^{-1}, much broader than the previously observed line widths between 1.7 and 2.1 km s^{-1} for CH_3OH and between 1.3 and 1.9 km s^{-1} for $NH_3(1,1)$ and $NH_3(2,2)$ (Beuther et al. 2005). Table 4 lists the observed line widths as well as the upper level excitation temperatures E_u/k and the critical densities n_{crit} for all observed absorption lines. The other extreme of the line-widths distribution is the line width of the ionized gas observed in the H76α line Δv = 32.0 km s^{-1} (de Pree et al. 1995).

Inspecting the values in Table 4 one can discern two trends: the first is the distinction between the broad line width and high critical density line HCN versus the small line width and low critical density lines from NH_3 and CH_3OH. In addition, within the low critical density molecules, one can tentatively identify a correlation between increasing E_u/k and increasing line width. Although judging from the errors this correlation is less clear, it remains suggestive.

There are different possibilities for explaining such trends: The picture of an expanding UCHII region[1] (Beuther et al. 2005) in its surrounding envelope implies that closer to the UCHII region surface the molecular densities and temperatures are higher than farther outside. Therefore, spectral lines tracing higher densities around an expanding UCHII region are expected to exhibit broader line widths because their emitting gas is more directly impacted than the lower-density medium farther out. A similar explanation could hold for the different excitation temperature regimes as well. A point of caution is that the opacity of HCN is probably one to two orders of magnitude larger than that of, e.g., NH_3. While we do not detect any NH_3 satellite hyperfine structure lines in absorption implying low NH_3 opacities, we cannot infer that exactly for HCN. If the HCN(1−0) optical depth were that high that it could not trace the dense gas regions close to the expanding UCHII region, then the above picture could hardly hold. Another explanation is based on the enhancement of HCN in the molecular outflow. Although the outflow does not emanate from the UCHII region but from the neighboring mm continuum source(s), de Pree et al. (1995) found a velocity gradient in the ionized gas similar to that of the molecular outflow. They suggested that the molecular outflow(s) in the region may well disturb the velocity field of the UCHII region and produce the velocity gradient this way. Since HCN is known to be abundant in molecular outflows (see also IRAS 18566+0408, Zhang et al. 2007, and IRAS 20126+4104, Su et al. 2007) a similar effect could explain the broad HCN(1−0) line widths toward the UCHII region. However, the 1st and 2nd moment maps (peak velocities and line widths) of the HCN(1−0) absorption presented in Fig. 10 (bottom panels) show no velocity gradient but a peak of the line-width distribution close to the center of the UCHII region. This is counter-intuitive for the outflow picture and suggests that the line-width differences are caused by the expanding UCHII region, possibly in a fashion comparable to that proposed above. Nevertheless, without knowing the optical depth of the HCN(1−0) line we cannot distinguish between the two scenarios.

3.2. NGC 6334I(N)

3.2.1. Millimeter continuum emission

Figure 2 (top-left panel) presents the 3.4 mm continuum emission toward NGC 6334I(N). In contrast to NGC 6334I, where we only see the UCHII region in the 3.4 mm continuum, toward

[1] In contrast to the previous CH_3OH and NH_3 absorption lines that showed additional blue-shifted emission indicative of expanding gas around the UCHII region (Beuther et al. 2005), the HCN data do not exhibit any clear expansion or infall signature.

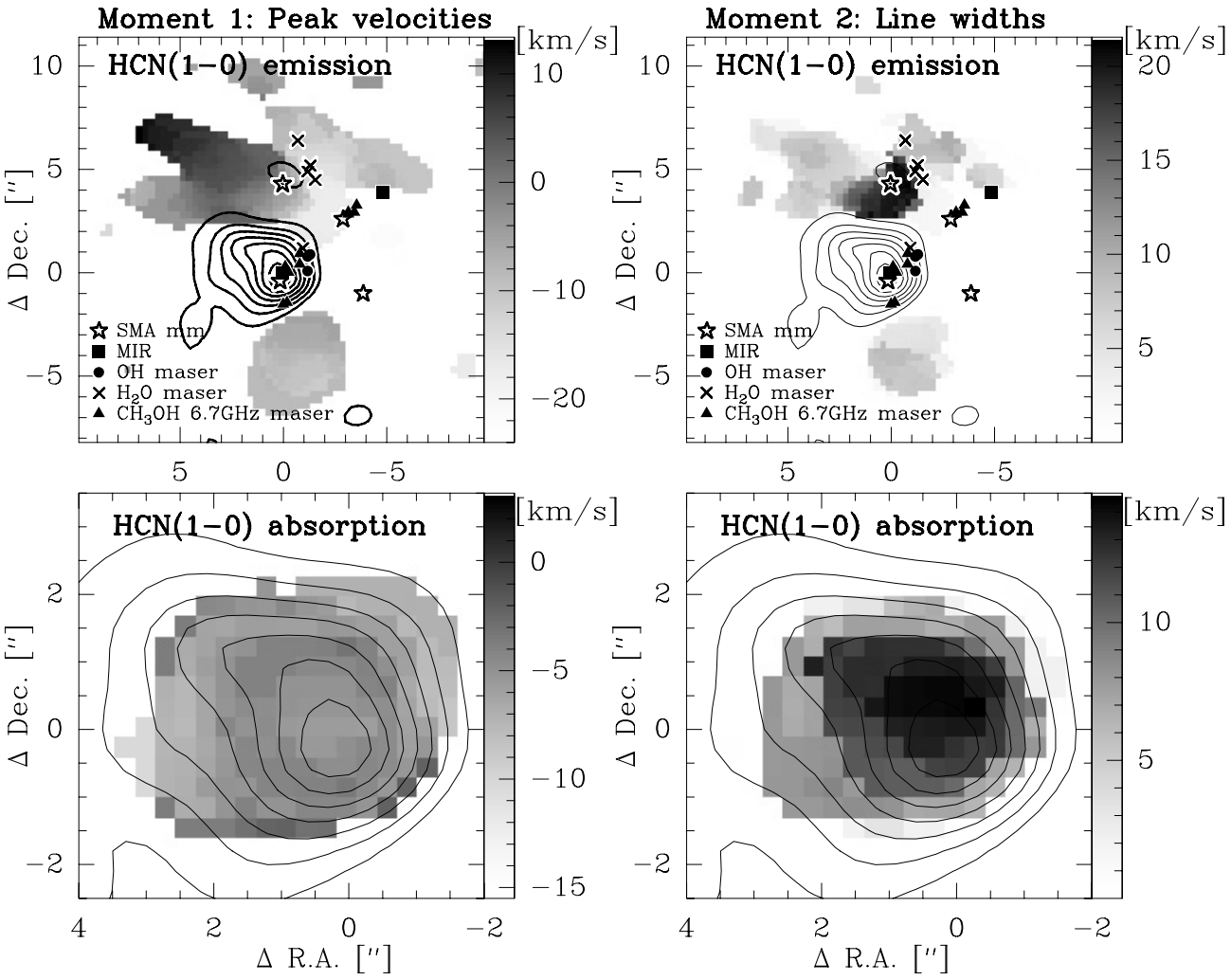

Fig. 10. Moment maps of HCN(1−0) toward NGC 6334I. *The left and right columns* present the first and second moments (peak velocities and line widths), respectively. *The top-row* shows the moments for the emission of the outflow and ambient gas, whereas the *bottom-row* presents the corresponding parameters for the absorption features toward the UCHII region. The contours present the 3.4 mm continuum emission in 3σ contour levels ($3\sigma \sim 69$ mJy beam^{-1}). The markers are the same as in Fig. 1.

NGC 6334I(N) we detect four out of seven previously identified protostellar 1.4 mm dust continuum condensations (Hunter et al. 2006) above a 5σ level of 13 mJy beam^{-1}. The peak fluxes $S_{\rm peak}$(3.4 mm) of the four sources, mm1 to mm3 and mm6, are listed in Table 5. Emission features below 5σ are not considered further. The 3.4 mm peak associated with mm1 is the strongest and shows an additional extension toward the northwestern 1.4 mm source mm5. In contrast to that, the 1.4 mm peak mm4, which is associated with cm continuum and CH_3OH class II maser emission, is not detected in our data above the 5σ level.

For a better comparison of the 3.4 mm fluxes with the previously observed 1.4 mm observations, we re-imaged the 1.4 mm data with exactly the same synthesized beam of 2.6″×1.8″ (position angle of 84 degrees from north). Figure 11 presents an overlay of the SMA 1.4 mm data with the ATCA 3.4 mm data at this same spatial resolution. While mm1 and mm6 are clearly separated in both wavelength bands, it is interesting to note that mm2 and mm3 merge in the 1.4 mm image at the reduced lower spatial resolution. The corresponding 1.4 mm peak fluxes are listed in Table 5. For the well separated sources mm1 and mm6 we can estimate the spectral indices α between both bands now, the derived values are 3.7 and 3.1, respectively (Table 5).

Recently Rodríguez et al. (2007) showed that the cm emission from NGC 6334I(N) is caused by free-free emission, whereas shortward of 7 mm wavelength the spectral energy distribution is dominated by dust continuum emission. In the Rayleigh-Jeans limit, the flux S scales with $S \propto \nu^{2+\beta}$ where β is the dust opacity index. With the measured spectral index α, we have dust opacity indices of 1.7 and 1.1 for mm1 and mm6, respectively. While the β value of mm1 is consistent with often observed values between 1.5 and 2, it is lower for mm6. Although the synthesized beams of both maps are the same, the uv-coverage was not during the observations. Furthermore, the continuum maps show a more peaked morphology toward mm1 than toward mm6. Thus, it is possible that mm6 has more extended structure and that this may be sampled better by the ATCA observations, possibly accounting for the observed lower values of α and β toward mm6. However, it is also feasible that physical reasons are responsible for this effect because a decreasing β can be attributed to grain growth in circumstellar disks as well (e.g., Beckwith et al. 1990). Nevertheless, in this scenario, it appears surprising that mm1, which likely drives an outflow and hence probably contains an accretion disk, has a value of β close to the interstellar medium values, whereas the source mm6, that does not exhibit clear signs of ongoing star formation, shows

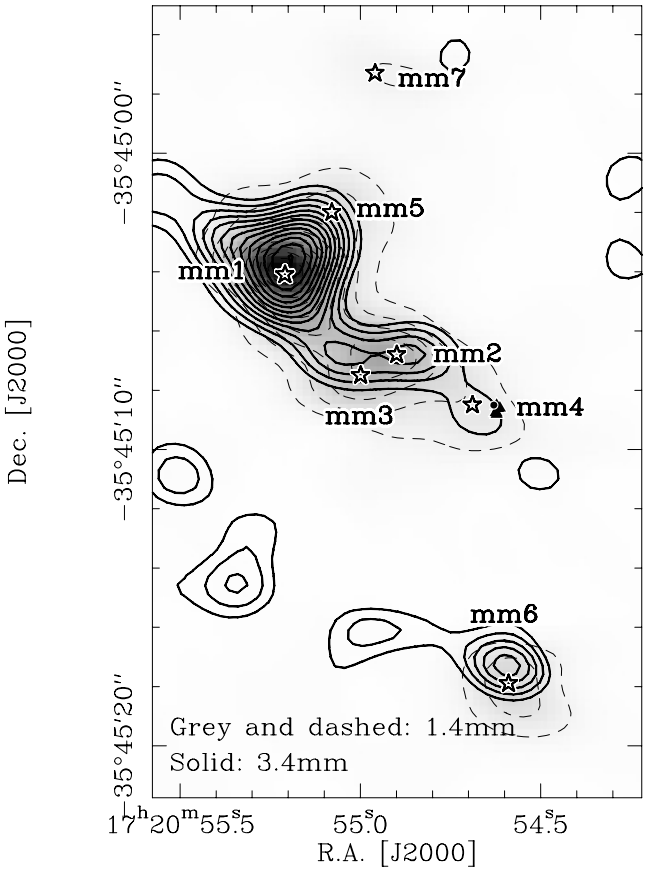

Fig. 11. Overlay of the SMA 1.4 mm continuum map (grey-scale with dashed contours) with the ATCA 3.4 mm map (solid contours) at the same angular resolution of 2.6″ × 1.8″. The 1.4 mm data are contoured from 10 to 90% of the peak emission (1077 mJy beam^{-1}). The 3.4 mm emission is contoured in 2σ steps (2σ(3.4mm) ∼5.2 mJy beam^{-1}. The synthesized beam of both images is the same with 2.6″ × 1.8″ (position angle of 84 degrees from north).

a lower value. Low α values could in principle also be caused by high optical depth or an early high-frequency turnover of the Planck-function caused by the low temperatures. However, the Planck-turnover of even a cold core starts changing the slope of the Rayleigh-Jeans part of the spectral energy distribution usually only above 350 GHz (e.g., Beuther et al. 2007a), and high optical depth compared to mm1 appears unlikely as well. Therefore, spatial filtering as well as physical effects could produce the low α toward mm6, but we cannot set better constraints here.

It should be noted that the spectral indices we find between 3.4 and 1.3 mm are larger than those derived previously by Rodríguez et al. (2007) based on VLA 7 mm data and the 1.3 mm data by Hunter et al. (2006). They find α of ∼2.4 for both sources mm1 and mm6. A potential explanation for this discrepancy can arise from different dust components traced by the various arrays. While the VLA 7 mm observations could be dominated by a compact dusty disk-component that remains optically thick at shorter wavelengths, the 3.4 and 1.4 mm data are likely dominated by the larger-scale optically thin envelope. This envelope with spectral indices between 3.1 and 3.7 (for mm1 and mm6) is weak and below the detection limit at 7 mm, which can cause the non-detection of any large-scale emission in the VLA data. A general word of caution should be added that comparing fluxes from different interferometers may be unreliable because

Table 5. Millimeter continuum parameters for NGC 6334I(N).

Source	$S_{\rm peak}$(3.4 mm) [mJy/beam]	$S_{\rm peak}$(1.4 mm) [mJy/beam]	α
mm1	36.6	1077	3.7
mm2	14.2	524[a]	
mm3	14.2	524[a]	
mm6	17.1	285	3.1

[a] The sources mm2 and mm3 are merged in the 1.4 mm dataset.

spatial filtering usually affects the fluxes of most measurements. Reducing datasets with similar uv-coverage and the same synthesized beam, as we have done here for the 3.4 and 1.4 mm data, helps to minimize this problem.

3.2.2. Dense gas traced by CH_3CN

The dense gas traced via the $CH_3CN(5_K–4_K)$ K-ladder exhibits two prominent peaks associated with the two main mm continuum sources mm1 and mm2 (Fig. 2). There is an additional tentative 3σ CH_3CN peak toward the mm peak mm4 associated with the cm and CH_3OH maser position, however, we refrain from further interpretation of this because the map shows negative features due to the incomplete uv-sampling and hence poor deconvolution on a comparable level. The other 1.4 and 3.4 mm continuum sources are not detected in the CH_3CN emission. This indicates that the average densities and/or abundances at those other mm positions are likely lower than the critical densities of the $CH_3CN(5_K–4_K)$ lines of a few times 10^5 cm^{-3} (Table 1). Based on this, one can speculate that except for the sources mm1, mm2 and mm4, all other mm continuum peaks may still be in a pre-stellar phase prior to active star formation.

Figure 12 presents the whole CH_3CN K-ladder spectrum extracted from the data-cube toward the two peak positions, and we again detect all K-components in both sources. The spectrum toward mm1 suffers from very high opacity problems as already outlined for NGC 6334I (Sect. 3.1.2), prohibiting any temperature estimate. However, for mm2 the situation is slightly different and temperature estimates become feasible. Again using the XCLASS software, we produced model spectra, and the $CH_3CN(5_K–4_K)$ spectrum can be fitted with temperatures in the regime of 170 ± 50 K. Such high temperatures additionally confirm the hot core-like nature of these sub-sources within the overall still relatively cold region NGC 6334I(N) (e.g., Gezari 1982).

Since previous $NH_3(6,6)$ observations showed a double-horn spectral profile toward mm1 (Beuther et al. 2007b), which could potentially be produced by an underlying accretion disk, we searched the high-K CH_3CN lines for rotation signatures as well. Figure 13 presents the 1st and 2nd moment maps of the $CH_3CN(5_4–4_4)$ line toward mm1. While we see a line width increase toward the center, which is indicative of more activity in the central region (e.g., rotation, outflow, infall), we cannot identify any obvious velocity gradient. Therefore, the data do not allow a more detailed analysis of the previously proposed underlying disk.

3.2.3. A precessing outflow?

The HCN(1−0) emission suffers strongly from the missing short spacings as indicated by all the negative features seen in Fig. 2. The morphology of the remaining HCN emission structures nevertheless indicates that most of it is associated with the northeast southwest molecular outflow rather than with the perpendicular

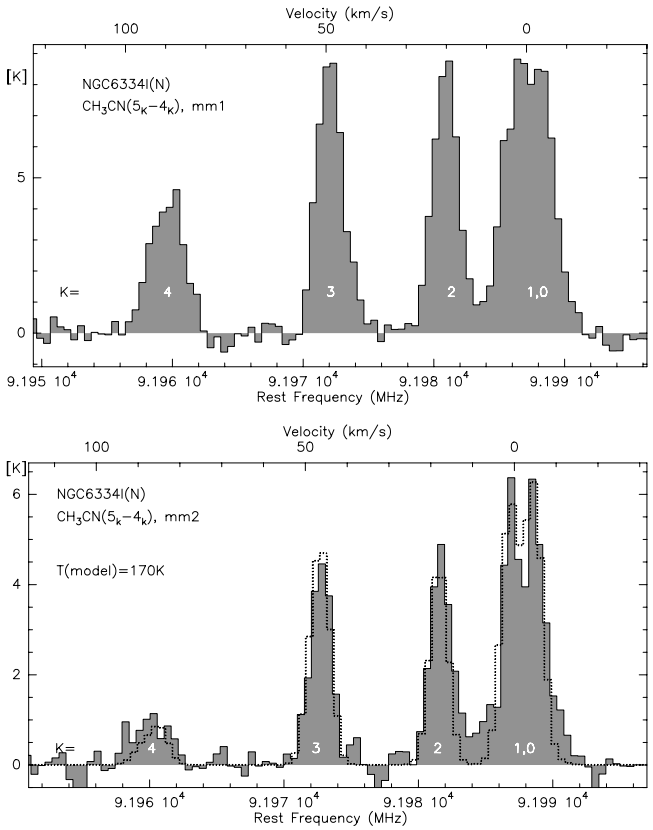

Fig. 12. $CH_3CN(5_K{-}4_K)$ spectra (K = 0...4) extracted toward the two CH_3CN peak positions in NGC 6334I(N) shown in Fig. 2. The dotted line in the lower panel shows a model spectrum created with XCLASS at a temperature of 170 K.

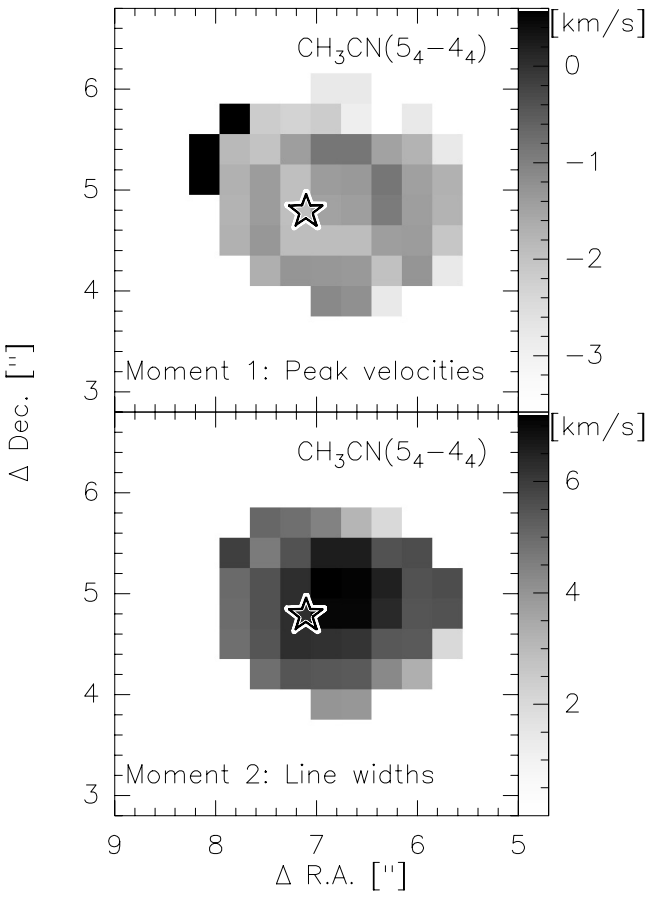

Fig. 13. Moment maps of $CH_3CN(5_K{-}4_K)$ toward NGC 6334I(N) mm1. The *top panel* shows the 1st moment (peak velocities) and the *bottom panel* the 2nd moment (line widths). The star marks the positions of the main mm continuum sources from Hunter et al. (2006).

one. Figure 14 shows the 1st and 2nd moment maps of the HCN emission, and the peak velocity and line-width distributions are a bit peculiar. The most red- and blue-shifted emission is centered around mm1 indicating that this is likely the driver of the northeast/southwest outflow. However, going farther to the northeast along the major outflow axis we find an inversion of the outflow velocities from red-shifted close to the protostar to blue-shifted at offsets around (12″/10″) from the phase center and then again red-shifted emission farther outward at offsets around (17″/13″). Regarding the line-width distribution, the 2nd moment map in Fig. 14 shows that the red-shifted parts of the northeastern outflow wing have systematically less broad lines than the blue-shifted part. This whole behavior is less pronounced in the southwestern outflow direction.

While the line-width differences are hard to explain, the change between blue-and red-shifted outflow emission is consistent with a picture in which a mean molecular outflow axis is close to the plane of the sky, and where the outflow precesses around that axis, producing in some region the receding red-shifted and in other regions the approaching blue-shifted emission. This precession picture is further supported by the spatial distribution of the HCN emission which resembles a reverse S-shaped morphology in the 1st moment map (Fig. 14).

The 2nd southeast northwest outflow is so far only observed at lower spatial resolution by Megeath & Tieftrunk (1999), who did not identify a driving source for it. While it could emanate from any other source, e.g., mm2, it is also possible that it originates from the vicinity of mm1. In the framework of precessing jets, a likely reason to cause the precession is the existence of multiple embedded objects (e.g., Fendt & Zinnecker 1998) which hence could also produce the quadrupolar outflow morphology (e.g., Gueth et al. 2001).

4. Conclusions and summary

Our 3.4 mm continuum and CH_3CN/HCN spectral line study of the massive twin cores NGC 6334I and I(N) reveals many new insights into that intriguing pair of massive star-forming regions. Both sets of spectral lines as well as the continuum emission are clearly detected toward both targets. While the continuum emission in NGC 6334I mainly follows the UCHII regions and the strongest protostellar 1.4 mm peak is detected only at a ~3σ level, in NGC 6334I(N), the 3.4 mm continuum emission traces four of the previously identified protostellar or pre-stellar condensations.

In both regions, the whole $CH_3CN(5_K{-}4_K)$ K-ladder from K = 0 to 4 is detected toward the strongest protostellar condensations. While the emission is in most cases so optically thick that temperature estimates are prohibited, toward the secondary mm peak in NGC 6334I(N) we can estimate a temperature of 170 ± 50 K. Toward all four detected CH_3CN emission sources, we find a correlation between increasing line width and increasing excitation temperature of the K components. Since increasing excitation temperatures are expected closer to the protostars, this implies more internal motions, e.g., outflow, infall or rotation, the closer one gets to the central protostar. Similar signatures are observed in the CH_3CN 2nd moment maps.

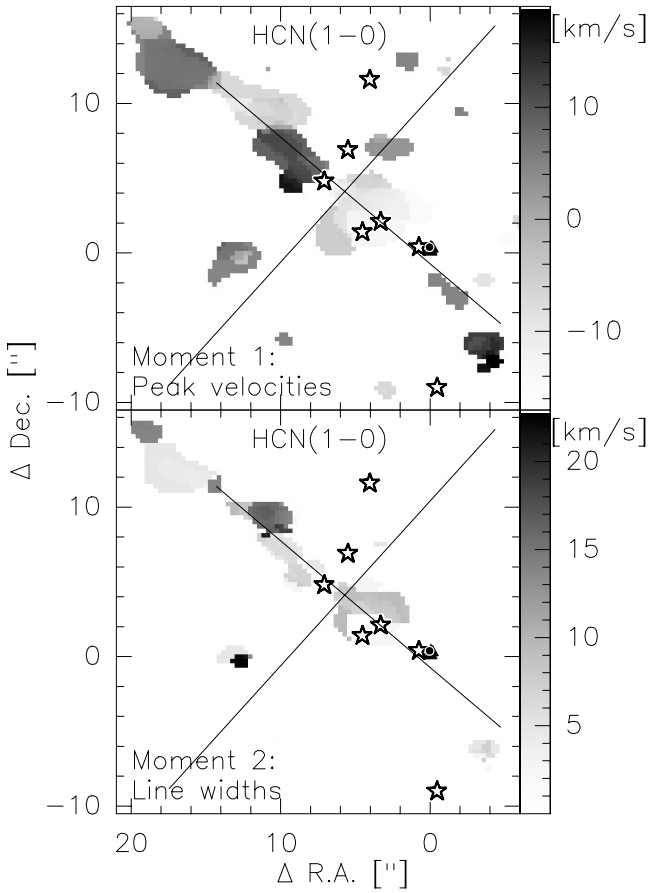

Fig. 14. Moment maps of HCN(1−0) toward NGC 6334I(N). The *top panel* shows the 1st moment (peak velocities) and the *bottom panel* the 2nd moment (line widths). The symbols correspond to the same phenomena as in Fig. 2.

To investigate potential rotation, we produced 1st moment maps toward all CH_3CN peaks, and fitted the channel peak positions toward mm1 in NGC 6334I to effectively increase the spatial resolution. We identify a velocity gradient toward mm1 in NGC 6334I that is oriented approximately perpendicular to the known large-scale outflow. This may be interpreted as a signature of a rotating structure, maybe associated with a massive accretion disk. While early rotation-disk claims for that region were on scales of the molecular outflow (Jackson et al. 1988), we are now reaching spatial scales on the order of a few hundred AU, much more reasonable for accretion disks (e.g., Yorke & Sonnhalter 2002; Krumholz et al. 2007). However, we have to stress that the rotation signatures are not conclusive yet because, e.g., an unresolved double-source could produce similar signatures. Further investigation at higher angular resolution are required to resolve this issue. While higher angular resolution images with the ATCA at 3 mm wavelengths are difficult because of decreasing phase stability with increasing baseline length, one may tackle that problem in some highly excited NH_3 lines in the 12 mm band. Furthermore, ALMA will allow the investigation of this source in much greater depth. Toward the previously suggested disk candidate in NGC 6334I(N) we cannot identify a similar velocity gradient.

In contrast to conventional wisdom that HCN traces the dense gas cores, we find it most prominently in the molecular outflows of both massive star-forming regions. The velocity structure of the outflow in NGC 6334I is relatively normal and follows the well-known Hubble-law for molecular outflows. In addition to that, we find the broadest HCN line width toward the main mm continuum peak mm1. In contrast to the previously found elongation of $NH_3(6,6)$ maser emission indicating that mm2 could drive the molecular outflow, these data suggest that mm1 harbors the outflow driving source. However, it is also possible that there are two molecular outflows with different properties that are preferentially detected in different tracers (HCN in this work and CO for the previous larger-scale outflow detection at a slightly different position-angle). The velocity structure of the NGC 6334I(N) outflow is more peculiar. There we find a change between blue- and red-shifted outflow emission on one side of the outflow. Taking into account the additionally bended morphology of that outflow, a possible explanation for this velocity structure is a precessing outflow close to the plane of the sky.

Furthermore, HCN exhibits a broad absorption feature with a line width of $\sim$15.4 km s^{-1} toward the UCHII region in NGC 6334I. Comparing the line width of the previously observed absorption features of NH_3 and CH_3OH, which are on the order of 2 km s^{-1}, with the HCN line width as well as the line width observed in the ionized gas of $\sim$32 km s^{-1}, two explanations are possible to explain the different line widths. The velocity gradient identified in the ionized gas indicates that it may be influenced by the molecular outflow close by. If the opacity of HCN were very large it traced only the outer gas layers around the UCHII region and could also be influenced by the outflow. On the other hand, NH_3 is optically thin based on the absent absorption in the hyperfine satellite lines. If HCN were optically thin as well, another possible explanation would be based on the different critical densities of the various molecules: In the picture of an expanding UCHII region, the densities close to the UCHII region surface should be higher than those farther outside. Hence HCN may trace the gas closer to the expanding UCHII region and is then much stronger affected by the expansion process that the lower-density regions farther out that are traced by NH_3 and CH_3OH. To differentiate between both models, observations of a rarer HCN isotopologue are required to derive its optical depth.

Acknowledgements. We like to thank Peter Schilke for providing the XCLASS software to model the CH_3CN spectra. Furthermore, we appreciate the careful referee's report which helped improving the paper. H.B. acknowledges financial support by the Emmy-Noether-Program of the Deutsche Forschungsgemeinschaft (DFG, grant BE2578).

References

Bachiller, R., & Cernicharo, J. 1990, A&A, 239, 276
Beckwith, S. V. W., Sargent, A. I., Chini, R. S., & Guesten, R. 1990, AJ, 99, 924
Beuther, H., Thorwirth, S., Zhang, Q., et al. 2005, ApJ, 627, 834
Beuther, H., Leurini, S., Schilke, P., et al. 2007a, A&A, 466, 1065
Beuther, H., Walsh, A. J., Thorwirth, S., et al. 2007b, A&A, 466, 989
Brogan, C. L., Chandler, C. J., Hunter, T. R., Shirley, Y. L., & Sarma, A. P. 2007, ApJ, 660, L133
Brooks, K. J., & Whiteoak, J. B. 2001, MNRAS, 320, 465
Carral, P., Kurtz, S. E., Rodríguez, L. F., et al. 2002, AJ, 123, 2574
Caswell, J. L. 1997, MNRAS, 289, 203
Comito, C., Schilke, P., Phillips, T. G., et al. 2005, ApJS, 156, 127
De Buizer, J. M., Radomski, J. T., Piña, R. K., & Telesco, C. M. 2002, ApJ, 580, 305
de Pree, C. G., Rodriguez, L. F., Dickel, H. R., & Goss, W. M. 1995, ApJ, 447, 220
Downes, T. P., & Ray, T. P. 1999, A&A, 345, 977
Fendt, C., & Zinnecker, H. 1998, A&A, 334, 750
Forster, J. R., & Caswell, J. L. 1989, A&A, 213, 339
Gaume, R. A., & Mutel, R. L. 1987, ApJS, 65, 193
Gezari, D. Y. 1982, ApJ, 259, L29
Gueth, F., Schilke, P., & McCaughrean, M. J. 2001, A&A, 375, 1018
Hunter, T. R., Brogan, C. L., Megeath, S. T., et al. 2006, ApJ, 649, 888

Jackson, J. M., Ho, P. T. P., & Haschick, A. D. 1988, ApJ, 333, L73
Kogan, L., & Slysh, V. 1998, ApJ, 497, 800
Kraemer, K. E., & Jackson, J. M. 1995, ApJ, 439, L9
Kraemer, K. E., & Jackson, J. M. 1999, ApJS, 124, 439
Kratter, K. M., & Matzner, C. D. 2006, MNRAS, 373, 1563
Krumholz, M. R., Klein, R. I., & McKee, C. F. 2007, ApJ, 656, 959
Kurtz, S., Churchwell, E., & Wood, D. O. S. 1994, ApJS, 91, 659
Lee, C., Stone, J. M., Ostriker, E. C., & Mundy, L. G. 2001, ApJ, 557, 429
Leurini, S., Schilke, P., Parise, B., et al. 2006, A&A, 454, L83
Loren, R. B., & Mundy, L. G. 1984, ApJ, 286, 232
Müller, H. S. P., Thorwirth, S., Roth, D. A., & Winnewisser, G. 2001, A&A, 370, L49
McCutcheon, W. H., Sandell, G., Matthews, H. E., et al. 2000, MNRAS, 316, 152
Megeath, S. T., & Tieftrunk, A. R. 1999, ApJ, 526, L113
Moran, J. M., & Rodríguez, L. F. 1980, ApJ, 236, L159
Neckel, T. 1978, A&A, 69, 51
Norris, R. P., Whiteoak, J. B., Caswell, J. L., Wieringa, M. H., & Gough, R. G. 1993, ApJ, 412, 222
Olmi, L., Cesaroni, R., & Walmsley, C. M. 1993, A&A, 276, 489
Pei, C. C., & Zeng, Q. 1995a, Acta Astron. Sinica, 36, 215
Pei, C. C., & Zeng, Q. 1995b, Acta Astron. Sinica, 36, 20
Persi, P., Tapia, M., Roth, M., Gómez, M., & Marenzi, A. R. 2005, in IAU Symp. 291, ed. R. Cesaroni, M. Felli, E. Churchwell, & M. Walmsley
Poynter, R. L., & Pickett, H. M. 1985, Appl. Opt., 24, 2235
Reid, M. J., Schneps, M. H., Moran, J. M., et al. 1988, ApJ, 330, 809
Rodríguez, L. F., Canto, J., & Moran, J. M. 1982, ApJ, 255, 103
Rodríguez, L. F., Zapata, L. A., & Ho, P. T. P. 2007, ApJ, 654, L143
Sandell, G. 2000, A&A, 358, 242
Schilke, P., Comito, C., Thorwirth, S., et al. 2006, A&A, 454, L41
Schöier, F. L., van der Tak, F. F. S., van Dishoeck, E. F., & Black, J. H. 2005, A&A, 432, 369
Shu, F. H., Ruden, S. P., Lada, C. J., & Lizano, S. 1991, ApJ, 370, L31
Smith, M. D., Suttner, G., & Yorke, H. W. 1997, A&A, 323, 223
Sollins, P. K., & Megeath, S. T. 2004, AJ, 128, 2374
Straw, S. M., & Hyland, A. R. 1989, ApJ, 340, 318
Su, Y.-N., Liu, S.-Y., Chen, H.-R., Zhang, Q., & Cesaroni, R. 2007, ApJ, 671, 571
Tapia, M., Persi, P., & Roth, M. 1996, A&A, 316, 102
Thorwirth, S., Winnewisser, G., Megeath, S. T., & Tieftrunk, A. R. 2003, in Galactic Star Formation Across the Stellar Mass Spectrum, ASP Conf. Ser., 287, 257
Tielens, A. G. G. M. 2005, The Physics and Chemistry of the Interstellar Medium (Cambridge University Press)
Walsh, A. J., Burton, M. G., Hyland, A. R., & Robinson, G. 1998, MNRAS, 301, 640
Walsh, A. J., Longmore, S. N., Thorwirth, S., Urquhart, J. S., & Purcell, C. R. 2007, MNRAS, 382, L35
Yorke, H. W., & Sonnhalter, C. 2002, ApJ, 569, 846
Zhang, Q., Sridharan, T. K., Hunter, T. R., et al. 2007, A&A, 470, 269